High oxygen pressure floating zone growth and crystal structure of the metallic nickelates $R_4Ni_3O_{10}$ (R = La, Pr)

Junjie Zhang,[1,2,*] Hong Zheng,[1] Yu-Sheng Chen,[3] Yang Ren,[4] Masao Yonemura,[5] Ashfia Huq,[6] and J. F. Mitchell[1,†]

[1]*Materials Science Division, Argonne National Laboratory, Argonne, Illinois 60439, USA*

[2]*Materials Science and Technology Division, Oak Ridge National Laboratory, Oak Ridge, Tennessee 37831, USA and Institute of Crystal Materials & State Key Laboratory of Crystal Materials, Shandong University, Jinan, Shandong 250100, China*

[3]*ChemMatCARS, The University of Chicago, Argonne, Illinois 60439, USA*

[4]*X-ray Science Division, Advanced Photon Source, Argonne National Laboratory, Argonne, Illinois 60439, USA*

[5]*Institute of Materials Structure Science, High Energy Accelerator Research Organization, 1-1 Oho, Tsukuba, Ibaraki 305-0801, Japan and Sokendai (The Graduate University for Advanced Studies), Shirakata 203-1, Tokai, Naka 319-1106, Japan*

[6]*Neutron Scattering Science Directorate, Oak Ridge National Laboratory, Oak Ridge, Tennessee 37831, USA*

(Received 7 April 2019; revised 6 June 2020; accepted 13 July 2020; published 13 August 2020)

Single crystals of the metallic Ruddlesden-Popper trilayer nickelates $R_4Ni_3O_{10}$ (R = La, Pr) were successfully grown using an optical-image floating zone furnace under oxygen pressure (pO_2) of 20 bar for $La_4Ni_3O_{10}$ and 140 bar for $Pr_4Ni_3O_{10}$. A combination of synchrotron and laboratory x-ray single-crystal diffraction, high-resolution synchrotron x-ray powder diffraction and measurements of physical properties revealed that $R_4Ni_3O_{10}$ (R = La, Pr) crystallizes in the monoclinic $P2_1/a$ ($Z = 2$) space group at room temperature, and that a metastable orthorhombic phase (*Bmab*) can be trapped by postgrowth rapid cooling. Both $La_4Ni_3O_{10}$ and $Pr_4Ni_3O_{10}$ crystals undergo a metal-to-metal transition (MMT) below room temperature. In the case of $Pr_4Ni_3O_{10}$, the MMT is found at 157.6 K. For $La_4Ni_3O_{10}$, the MMT depends on the lattice symmetry: 147.5 K for *Bmab* vs 138.6 K for $P2_1/a$. Lattice anomalies were found at the MMT that, when considered together with the pronounced dependence of the transition temperature on subtle structural differences between *Bmab* and $P2_1/a$ phases, demonstrate a not insignificant coupling between electronic and lattice degrees of freedom in these trilayer nickelates.

DOI: 10.1103/PhysRevMaterials.4.083402

I. INTRODUCTION

Quasi-two-dimensional (2D) transition metal oxides with strong electron correlations have attracted considerable attention due to their collective properties such as high-temperature superconductivity in cuprates [1–5], colossal magnetoresistance in manganites [6], and metal-insulator transitions in nickelates [7]. Ordering of charge, spin, and orbital are important phenomena underlying these exotic physical properties [1–5,8]. In particular, charge order, or charge density wave (CDW) order, has been established as an instability of the underdoped cuprate superconductors [9]. Charge order has also been found in noncopper transition metal oxides containing mixed valence states, such as Mn^{3+}/Mn^{4+} [10], Ni^{2+}/Ni^{3+} [11], Ni^{1+}/Ni^{2+} [12], Fe^{2+}/Fe^{3+} [13], and Co^{2+}/Co^{3+} [14]. One notable characteristic of charge order in these latter systems is their insulating ground state, instead of the metallic state found in cuprates [8]. The metallic, mixed-valent Ruddlesden-Popper trilayer nickelates, $R_4Ni_3O_{10}$ (R = La, Pr, and Nd), nominally contain Ni^{2+}/Ni^{3+}; the average valence state is 2.67+, which can be thought of as 0.67 holes doped into a background of Ni^{2+}. Such hole doping, if mapped onto the cuprates, would lie far into the overdoped regime, which is generally regarded as conventional Fermi liquid possessing no collective electronic order. However, Peng *et al.* recently discovered charge order in the overdoped cuprate $(Bi, Pb)_{2.12}Sr_{1.88}CuO_{6+\delta}$ without nesting or pseudogap features [15]. It is thus relevant to establish if the ground state of these metallic trilayer nickelates expresses CDW order to better delimit what is a growing body of work exploring the connections between nickelates and cuprates, most dramatically expressed through the recent discovery of superconductivity in thin films of $Nd_{0.8}Sr_{0.2}NiO_2$ [16].

The trilayer nickelates $R_4Ni_3O_{10}$ (R = La, Pr) have been reported to undergo metal-to-metal transitions (MMTs, $\approx$140 K for $La_4Ni_3O_{10}$ and $\approx$160 K for $Pr_4Ni_3O_{10}$ and $Nd_4Ni_3O_{10}$) [17–24]. The transition was ascribed by Zhang and Greenblatt to CDW-driven instabilities [18]. Later, Seo *et al.* published one-electron, tight-binding band structure calculations (at the extended Hückel level), predicting a CDW nesting vector of $\boldsymbol{q} = 0.3\boldsymbol{a}^*$ or $0.3\boldsymbol{b}^*$ [25,26]. However, direct evidence of CDW formation, e.g., the observation of superlattice lines by x-ray, neutron, or electron diffraction, has not been reported in polycrystalline samples [18,21,27]. An obvious next step would be study of single crystals. However, a challenge to crystal growth originates from the fact that $La_4Ni_3O_{10}$ decomposes to $La_3Ni_2O_7$ and NiO before it melts, as can be seen from the La-Ni-O phase diagram in Ref. [28]. The advent of high pO_2 floating zone crystal growth capabilities has overcome this problem, and crystals of $R_4Ni_3O_{10}$ have been grown by us [12,29,30] and others [23]. Indeed, using these crystals in a combined x-ray and neutron scattering

*junjie@sdu.edu.cn
†mitchell@anl.gov

study, we have recently discovered compelling evidence of the simultaneous formation of intertwined charge and spin density waves in the metallic oxide, $La_4Ni_3O_{10}$ [31].

Despite considerable focus on these materials, the crystal structure of $R_4Ni_3O_{10}$ (R = La, Pr, and Nd) above the MMT still remains under debate. Four different space groups have been proposed in the literature: (i) *Bmab* (alternate setting of *Cmce*), as reported by Tkalich *et al.* [17], Ling *et al.* [21], and Voronin *et al.* [32]. (ii) *Imm*2: Zhang and Greenblatt reported *Fmmm* from powder x-ray diffraction, but their electron diffraction patterns show that the space group symmetry is lower than F or C, and the highest-symmetry space group possible is *Imm*2 [18]. (iii) $P2_1/a$ ($Z = 4$): Olafsen *et al.* reported $P2_1/a$ [$a = 5.3675(2)$ Å, $b = 5.4548(2)$ Å, $c = 27.433(1)$ Å, $\beta = 90.312(2)^\circ$] for $Nd_4Ni_3O_{9.85}$ based on refinement of powder neutron diffraction data at 298 K [33]. Later, Nagell *et al.* [34], Kumar *et al.* [35], and Li *et al.* [24] refined their powder diffraction data using this space group. Notably, the above three structures were obtained from Rietveld refinements on powder diffraction data, which suffer from significant peak broadening arising from anisotropic strain and stacking faults [34,36]. (iv) $P2_1/a$ ($Z = 2$): Huangfu *et al.* reported $P2_1/a$ [$a = 5.3771(5)$ Å, $b = 5.4549(3)$ Å, $c = 14.028(2)$ Å, $\beta = 100.910(9)^\circ$] from lab x-ray single-crystal diffraction of $Pr_4Ni_3O_{10}$ at 293 K [23]. Recently, Huangfu *et al.* investigated phase transition in $Ln_{4-x}Ln'_xNi_3O_{10}$ (Ln and Ln'=La, Pr and Nd, $x = 0$, 1, 2, and 3) polycrystalline powders using this structural model [37]. Whether $La_4Ni_3O_{10}$ and $Nd_4Ni_3O_{10}$ crystallize in the same $P2_1/a$ ($Z = 2$) is an open question.

In this paper, we report single-crystal growth of $R_4Ni_3O_{10}$ (R = La, Pr) and establish their crystal structures above the MMT. The outline of the present paper is as follows. First, we present the successful growth of bulk single crystals of $R_4Ni_3O_{10}$ (R = La, Pr) using the high-pressure optical-image floating zone technique. The obtained stable phases with increasing pO_2 follow along a progression with n in $La_{n+1}Ni_nO_{3n+1}$. Second, we investigate the physical properties including resistivity, magnetic susceptibility, and heat capacity of $R_4Ni_3O_{10}$, where we find $La_4Ni_3O_{10}$ exhibits an unexpected phase transition at $T_{MMT} = 147.5$ K in addition to the 138.6 K transition reported in the literature [19–21,35]. We attribute these transitions to metastable orthorhombic and stable monoclinic phases, respectively. In contrast, $Pr_4Ni_3O_{10}$ shows a single MMT at 157.6 K, consistent with a single-phase sample. Third, we determine the crystallographic structure above the MMT using synchrotron and lab x-ray single-crystal diffraction. Both $La_4Ni_3O_{10}$ with $T_{MMT} = 138.6$ K and $Pr_4Ni_3O_{10}$ crystalize in the monoclinic space group $P2_1/a$ ($Z = 2$) reported by Huangfu *et al.* for $Pr_4Ni_3O_{10}$ [23], while the $La_4Ni_3O_{10}$ with $T_{MMT} = 147.5$ K belongs to the orthorhombic structure *Bmab*. Fourth, we discuss annealing experiments on biphasic samples to address the question of the true thermodynamic phase of $R_4Ni_3O_{10}$ at room temperature, *Bmab* or $P2_1/a$. Finally, we summarize our findings.

II. EXPERIMENT

A. Solid-state reaction

Precursors for crystal growth were synthesized via standard solid-state reaction techniques. Stoichiometric amounts of La_2O_3 (Alfa Aesar, 99.99%) or Pr_6O_{11} (Alfa Aesar, 99.99%) and NiO (Alfa Aesar, 99.99%) were thoroughly ground. For $Pr_4Ni_3O_{10}$, an excess of 0.5%–1.5% NiO was added to compensate the loss during growth due to volatilization during growth at high pO_2 [38]. The mixture was then loaded into a Pt crucible and heated in air from room temperature to 1050 °C at a rate of 3 °C/min, allowed to dwell for 24 h, then furnace cooled to room temperature. The solid was then reground and sintered twice at 1050 °C using the procedures mentioned above. In the case of $La_4Ni_3O_{10}$, powder x-ray diffraction showed a phase mixture consisting of $La_4Ni_3O_{10}$, $La_3Ni_2O_7$, La_2NiO_4, La_2O_3, and NiO (see Fig. S1 of the Supplemental Material [39]).

B. High-pO_2 crystal growth

Crystals of $R_4Ni_3O_{10}$ (R = La, Pr) were successfully grown using a vertical optical-image floating zone furnace designed for operation at elevated gas pressure (150-bar Model HKZ, SciDre GmbH, Dresden). Precursor powders of $La_4Ni_3O_{10}$ were hydrostatically pressed into polycrystalline rods (length = 100mm, diameter = 8mm) and sintered for 24 h at 1400 °C to make a dense rod. $La_4Ni_3O_{10}$ crystals were grown directly from the sintered rod at $pO_2 = 20$ bar using a 3-kW xenon arc lamp to heat the zone. A similar procedure was applied to $Pr_4Ni_3O_{10}$ but severe cracking in the feed rod during growth resulted in melt zone loss. By reducing the sintering temperature to 1100 °C and making a less dense rod, the cracking issue was avoided. $Pr_4Ni_3O_{10}$ crystals were grown at $pO_2 = 140$ bar through two steps using a 5-kW xenon arc lamp. The first step was a fast pass (30–50 mm/h) to improve density. This was followed by a second growth at the same pressure with slow traveling rate, 5 mm/h. During growth, a flow rate of 0.1 l/min of oxygen was maintained. Feed and seed rods were counter-rotated at 27 and 20 rpm, respectively, to improve zone homogeneity.

C. Single-crystal structural determination

Single-crystal x-ray diffraction data were collected with a Bruker APEX2 area detector using lab x ray at room temperature ($\lambda = 0.710\,73$ Å) and using synchrotron radiation at 200 K at Beamline 15-ID-D at the Advanced Photon Source, Argonne National Laboratory. Single crystals were mounted to the tip of glass fibers and measured using a Bruker D8 diffractometer. Indexing was performed using Bruker APEX2 software [40]. Data integration and cell refinement were performed using SAINT, and multiscan absorption corrections were applied using the SADABS program [40]. The structure was solved by direct methods and refined with full matrix least-squares methods on F^2. All atoms of monoclinic $R_4Ni_3O_{10}$ (R = La, Pr) and La atoms of orthorhombic $La_4Ni_3O_{10}$ were modeled using anisotropic ADPs, and the refinements converged for $I > 2\sigma(I)$, where I is the intensity of reflections and $\sigma(I)$ is standard deviation. Calculations were performed using the SHELXTL crystallographic software package [41]. Details of crystal parameters, data collection, and structure refinement are summarized in Table I. Selected bond distances (Å) and angles (deg) are given in Table II. Further details of the crystal structure investigations

TABLE I. Crystallographic data for $R_4Ni_3O_{10}$ (R = La, Pr) above the metal-to-metal transition temperatures.

Empirical formula	$La_4Ni_3O_{10}$	$La_4Ni_3O_{10}$	$Pr_4Ni_3O_{10}$
Crystal system	Orthorhombic	Monoclinic	Monoclinic
Space group	*Bmab*	$P2_1/a$	$P2_1/a$
Temperature (K)	200(2)	200(2)	298(2)
Formula weight	891.77	891.77	899.77
a (Å)	5.4183(5)	5.4151(3)	5.3816(2)
b (Å)	5.4696(5)	5.4714(3)	5.4711(3)
c (Å)	27.946(2)	14.2277(7)	14.0284(6)
β (deg)	90	100.818(1)	100.646(2)
V (Å^3)	828.21(12)	414.05(4)	405.93(3)
Density (calculated) (g/cm^3)	7.152	7.153	7.361
Z	4	2	2
Radiation type	Synchrotron x-ray, 0.41328 Å	Synchrotron x-ray, 0.41324 Å	Mo $K\alpha$, 0.71073 Å
Crystal size (mm^3)	0.037 × 0.012 × 0.008	0.05 × 0.02 × 0.007	0.04 × 0.03 × 0.02
Absorption coefficient (mm^{-1})	5.633	5.634	30.367
Data collection diffractometer	15-ID-D, APS	15-ID-D, APS	Bruker APEX2
Absorption correction	Multiscan	Multiscan	Multiscan
Reflections collected	7381	7359	4934
Independent reflections	1064 (R_{int} = 0.0552)	1841 (R_{int} = 0.0334)	1239 (R_{int} = 0.0260)
θ range for data collection (deg)	2.325–21.470	0.847–21.298	1.477–31.293
F(000)	1568	784	800
Index ranges	$-8\leqslant h\leqslant 8$, $-8\leqslant k\leqslant 8$, $-36\leqslant l\leqslant 38$	$-9\leqslant h\leqslant 9$, $-9\leqslant k\leqslant 9$, $-22\leqslant l\leqslant 22$	$-7\leqslant h\leqslant 7$, $-7\leqslant k\leqslant 7$, $-19\leqslant l\leqslant 19$
Refinement method	Full-matrix least squares on F^2	Full-matrix least squares on F^2	Full-matrix least squares on F^2
Data, restraints, parameters	1064, 0, 29	1841, 0, 79	1239, 0, 79
Goodness of fit	1.097	1.118	1.121
$R_1/wR_2(I > 2\sigma)$	0.0595/0.1693	0.0284/0.0843	0.0341/0.0766
R_1/wR_2 (all)	0.0618/0.1720	0.0295/0.0859	0.0431/0.0802
Largest diff. peak and hole (e) (Å^{-3})	6.126 and −10.383	2.733 and −2.209	3.867 and −2.353

may be obtained from the joint CCDC/FIZ Karlsruhe online deposition service [42] by quoting the deposition number CSD 1999906–1999908.

D. Sample annealing

Under flowing oxygen, as-grown single crystals of $La_4Ni_3O_{10}$ were heated to 1000 °C at a rate of 200 °C/h, held for 12 h, and then cooled to 200 °C at a rate of 30 °C/h, and finally to room temperature by turning off the furnace. High pO_2 annealing was performed in a specially constructed annealing furnace (Model AHSO, SciDre GmbH, Dresden) under 20 bar oxygen pressure. Samples were held for 2 h at 950 °C or 1050 °C, and then quenched to room temperature.

E. Powder x-ray diffraction (PXRD)

Room-temperature PXRD was performed on a PANalytical X'Pert PRO diffractometer using Cu $K\alpha$ radiation (λ = 1.5418 Å). High-resolution PXRD data were collected at Beamline 11-BM in the range $0.5^\circ \leqslant 2\theta \leqslant 28^\circ$ with a step size of 0.001° and counting time of 0.1 s per step and a wavelength of $\lambda = 0.459\,003$ Å for $Pr_4Ni_3O_{10}$ and $\lambda = 0.414\,579$ Å for $La_4Ni_3O_{10}$. Samples were prepared by loading pulverized crystals into a Φ0.5-mm quartz capillary. The quartz capillary was then loaded inside a Φ0.8-mm Kapton capillary for installation on a magnetic sample base used by the beamline sample changer. The sample was spun continuously at 5600 rpm during data collection. An Oxford Cryostream 700 Plus N_2 gas blower was used to control temperature below room temperature. Diffraction patterns were recorded at room temperature first (1-h scan) and then on cooling from 296 to 100 K (10 min per scan, cooling rate of 0.3 K per min). The same sample of $La_4Ni_3O_{10}$ before and after annealing in flowing oxygen was measured at room temperature in the range $0.5^\circ \leqslant 2\theta \leqslant 50^\circ$ with a step size of 0.001° and counting time of 0.1 s per step and a wavelength of $\lambda = 0.414\,167$ Å. Temperature-dependent diffraction data above room temperature were collected at 50 °C−200 °C (at 50 °C intervals), 220 °C−380 °C (at 10 °C

TABLE II. Bond lengths of Ni-O in *Bmab*, $P2_1/a$ $La_4Ni_3O_{10}$, and $Pr_4Ni_3O_{10}$.

	Bmab$La_4Ni_3O_{10}$	$P2_1/a La_4Ni_3O_{10}$	$Pr_4Ni_3O_{10}$
Inner Ni of the trilayer (Å)	1.920(5)	1.925(3)	1.922(6)
	1.920(5)	1.925(3)	1.922(6)
	1.9354(9)	1.936(4)	1.957(7)
	1.9354(9)	1.936(4)	1.957(7)
	1.9354(9)	1.940(4)	1.957(7)
	1.9354(9)	1.940(4)	1.957(7)
Bond valence sum	3.01	2.98	2.89
Outer Ni of the trilayer (Å)	1.9238(6)	1.922(3)	1.922(6)
	1.9238(6)	1.927(3)	1.926(6)
	1.9359(6)	1.930(3)	1.934(6)
	1.9359(6)	1.941(3)	1.947(6)
	2.001(5)	1.991(3)	2.001(6)
	2.165(6)	2.170(3)	2.154(6)
Bond valence sum	2.70	2.70	2.69
Ni-O-Ni angle in the *ab* plane (deg)	171.6(3)	170.6(2)	167.8(4)
	171.8(3)	172.46(19)	165.1(4)
	168.0(5)	166.5(3)	157.3(4)
Ni-O-Ni angle out of the *ab* plane (deg)	165.6(4)	165.1(2)	158.1(4)

intervals), 430 °C−550 °C (at 10 °C intervals), 600 °C, and 650 °C with temperature controlled by a hot air blower. Data were analyzed with the Rietveld method using GSAS-II software [43]. The background at each temperature was fit using a Chebyshev polynomial (14 terms). Other refined parameters include scale factor, sample displacement perpendicular to beam, phase ratio, lattice parameters, atomic positions, isotropic atomic displacement parameters (all like atoms were grouped together), and profile shape parameters. Isotropic domain size and generalized microstrain models were used. Parametric sequential fitting was performed for temperature-dependent data.

F. Neutron powder diffraction (NPD)

Temperature-dependent NPD data were collected on a time-of-flight (TOF) Super High-Resolution Powder Diffractometer, Super HRPD [44,45] at the Material and Life Science Facility (MLF) in the Japan Proton Accelerator Research Complex (J-PARC). The powder sample was installed in a cylindrical vanadium cell of dimensions 6 mm in diameter, 55 mm in height, and 100 μm in thickness. All diffraction data were collected using all detectors in the range $10^\circ < 2\theta < 172^\circ$. The diffraction data from the backscattering bank ($150^\circ < 2\theta < 172^\circ$) were used for the analysis. Structural refinements were performed using Z-RIETVELD software [46,47].

G. Oxygen content

Oxygen content of $R_4Ni_3O_{10}$ (R = La, Pr) was determined by reduction in a $4\%H_2/N_2$ mixture on a thermogravimetric analysis (Mettler Toledo Model TGA/DSC 1). Pulverized samples (∼100 mg) taken from the crystal boule were placed into a 150-μl Al_2O_3 crucible and heated at a rate of 10 °C/min from room temperature to 900 °C, held for 5 h, and then cooled at 10 °C/min to room temperature (see Fig. S2 of the Supplemental Material [39]). Multiple blanks had been run previously to establish stability and buoyancy correction.

H. Heat capacity

Heat capacity measurements were performed on a Quantum Design PPMS in the temperature range of 1.8–300 K. Apiezon-N vacuum grease was employed to fix crystals to the sapphire sample platform. The specific heat contribution from sample holder platform and grease was determined before mounting sample and subtracted from the total heat capacity.

I. Magnetic susceptibility

Magnetic susceptibility measurements were performed on single crystals using a Quantum Design MPMS3 SQUID magnetometer. Single crystals were attached to a quartz holder using a minute amount of adhesive. ZFC-W (zero-field cooling with data collected on warming), FC-C (field cooling and data collected on cooling), and FC-W (field cooling and data collected on warming) data with magnetic field $H_{//}ab$ plane and $H_{\perp}ab$ were collected between 1.8 and 300 K under an external field of 0.4 T. In the ZFC-W protocol, the sample was cooled in zero field to 10 K at a rate of 35 K/min and then to 1.8 K at a rate of 2 K/min, and dc magnetization recorded on warming (2 K/min). In the FC-C and FC-W protocols, the magnetization was recorded (2 K/min) in a fixed field of 0.4 T. Isothermal field-dependent magnetization at 1.8 and 300 K with magnetic field $H_{//}ab$ plane and $H_{\perp}ab$ were measured in a field range of ±7 T following field cooling (10 K/min) under 7 T.

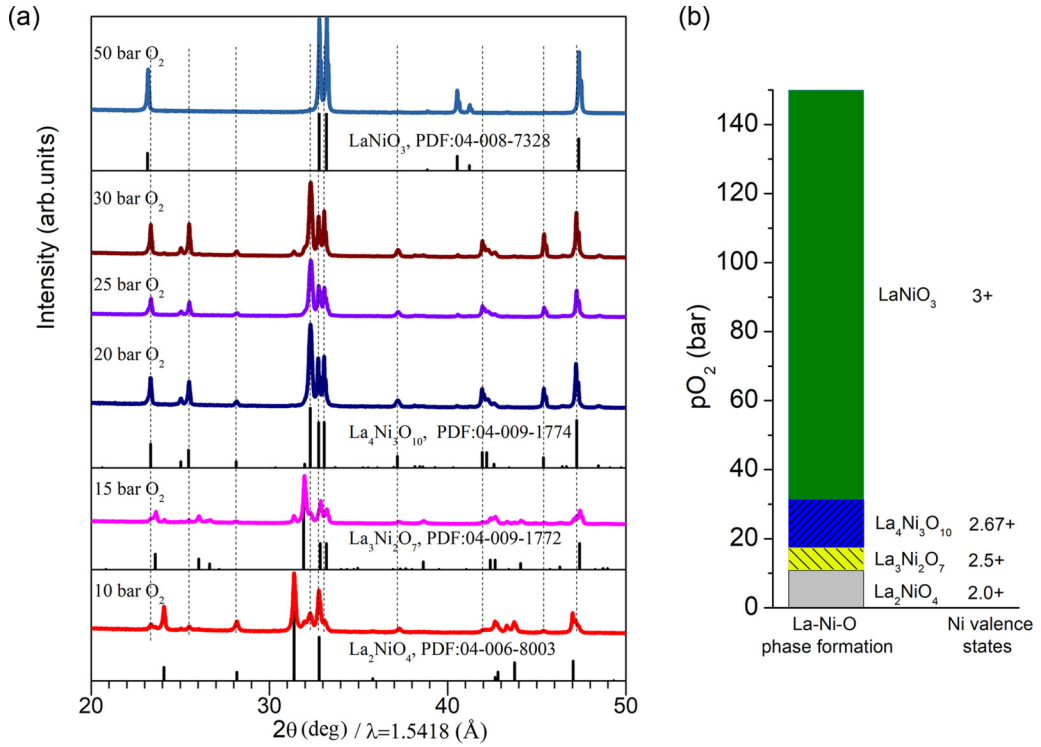

FIG. 1. Rapid cooling products from a melt of La_2O_3 : NiO = 2 : 3 at various oxygen pressures. (a) Powder x-ray diffraction patterns vs pO_2 with standard patterns of $La_{n+1}Ni_nO_{3n+1}$ (n = 1, 2, 3, and ∞) from the ICDD database shown as tick marks below the data. (b) Schematic drawing of empirical phase predominance as a function of pO_2.

J. Electrical resistivity

Resistivity of $La_4Ni_3O_{10}$ single crystals was measured using a four-terminal method while $Pr_4Ni_3O_{10}$ single crystals were measured using a six-terminal method [48,49] with contacts made by depositing gold pads. Temperature was controlled using the Quantum Design PPMS in the temperature range of 1.8–300 K.

III. RESULTS AND DISCUSSION

A. High pO_2 crystal growth

We first explored phase formation as a function of oxygen pressure by melting and rapid cooling materials with a starting composition of La_2O_3 : NiO = 2 : 3 (see Fig. S1 of the Supplemental Material [39]). At pO_2 = 0.21 bar O_2, $La_4Ni_3O_{10}$ decomposes to $La_3Ni_2O_7$, NiO, and O_2 at ∼1400 K based on the phase diagram reported by Zinkevich *et al.* [22,28]. The lack of a tie line to a liquid phase precludes growth of a single crystal from the melt at ambient pressure. Considering the high valence state of Ni (nominal +2.67), a highly oxidizing environment is expected to help stabilize the target phase. Figure 1(a) presents the lab powder x-ray diffraction patterns of the phases obtained by rapid cooling the melt at various pO_2 with La_2NiO_4, $La_3Ni_2O_7$, $La_4Ni_3O_{10}$, and $LaNiO_3$ as references. The data confirm that high pO_2 is crucial for the formation of various Ruddlesden-Popper nickelates and that the stable phases with increasing pressure follow along the progression with n in $La_{n+1}Ni_nO_{3n+1}$, i.e.; La_2NiO_4 was obtained at low pO_2, $La_3Ni_2O_7$ was the majority phase at ∼14 bar, $La_4Ni_3O_{10}$ was obtained when pO_2 is in the range of 16–30 bar (see Fig. S3 of the Supplemental Material [39]), and $LaNiO_3$ was the major phase at and above 50 bar. We have already reported the successful growth of metallic $LaNiO_{3-\delta}$ at 40 and 130 bar O_2 [50,51], as has Guo *et al.* [52] and Dey *et al.* [53]. Figure 1(b) schematically illustrates the oxygen pressure stability range for different phases. As expected, this is in line with nominal Ni oxidation states.

To optimize the pO_2 for $R_4Ni_3O_{10}$ (R = La, Pr) crystal growth, it is critical to use as high pO_2 as possible to suppress the formation of single-layer R_2NiO_4 and bilayer $R_3Ni_2O_7$, but low enough to avoid the perovskite phase, $RNiO_3$. We found a trace of $LaNiO_3$ at pO_2 = 25 bar for $La_4Ni_3O_{10}$ growth in lab x-ray powder diffraction patterns; thus, we adopted 20 bar pO_2 for crystal growth of $La_4Ni_3O_{10}$. The same procedure was applied to the case of Pr-Ni-O, and we found Pr_2NiO_4 formed at low pressure and $Pr_4Ni_3O_{10}$ above 100 bar O_2. We were unable to stabilize either the bilayer $Pr_3Ni_2O_7$ or the perovskite $PrNiO_3$ below the 150-bar limit of our furnace. The missing $Pr_3Ni_2O_7$ may reflect a very narrow pressure region of stability or an inversion of the stability ranges of $Pr_3Ni_2O_7$ and $Pr_4Ni_3O_{10}$ vis-à-vis the La counterparts. $PrNiO_3$ lies at pO_2 higher than 150 bar, as we recently reported for the single-crystal growth of this compound at ∼300 bar pO_2 [54]. For the crystal growth of $Pr_4Ni_3O_{10}$, we employed oxygen pressure of 140 bar.

To obtain high-quality single crystals of $R_4Ni_3O_{10}$ (R = La, Pr), we also investigated other growth parameters including traveling rates, feeding rates, rotation speeds, and post-growth cooling rates. We found that fast traveling rates, e.g., 30–50 mm/h, introduce second phases (e.g., La_2NiO_4) during

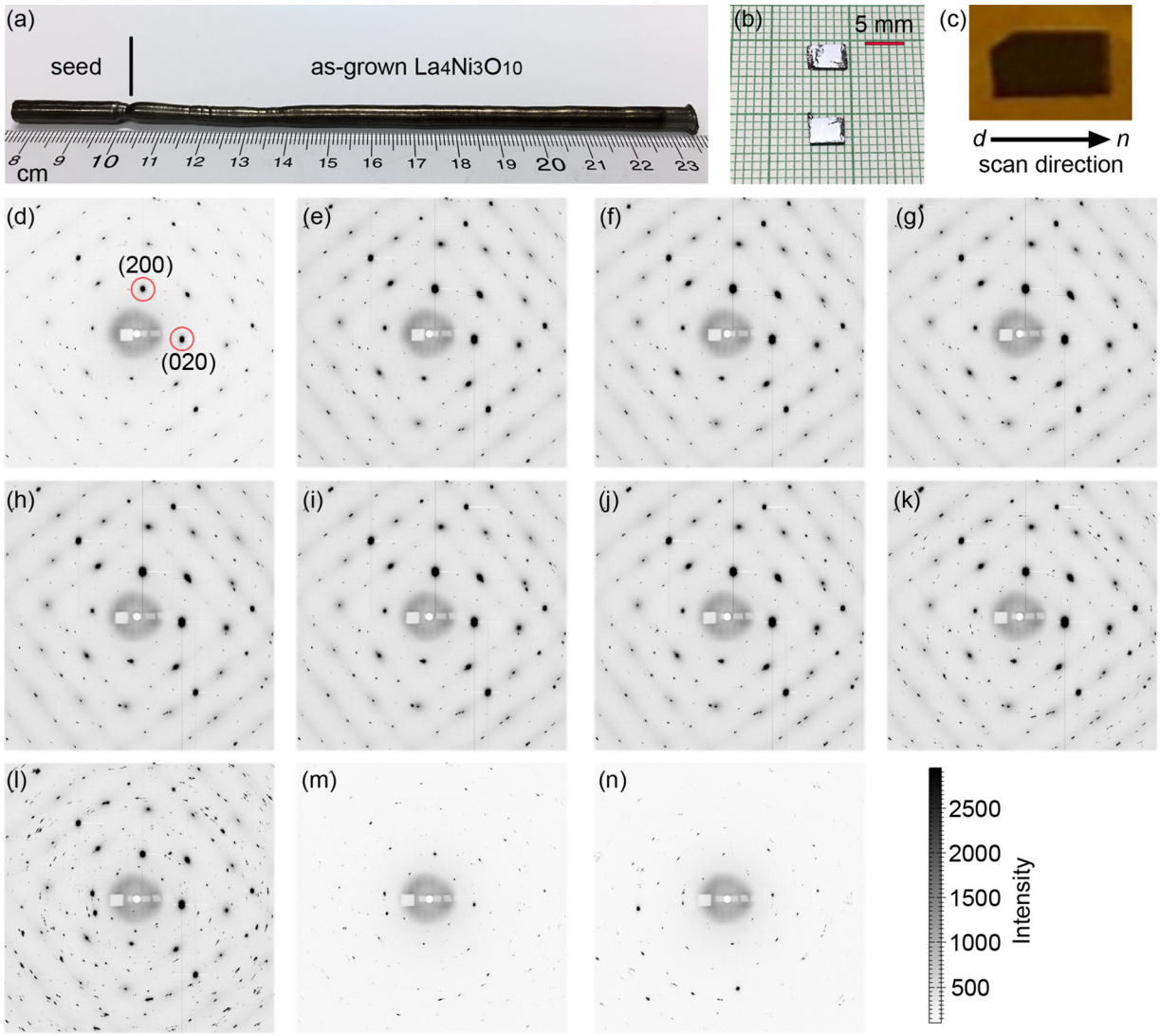

FIG. 2. High-energy synchrotron x-ray single-crystal diffraction from an as-grown $La_4Ni_3O_{10}$ crystal. (a) Photograph of as-grown boule with crystal growth direction parallel to the *ab* plane. (b) Cleaved $La_4Ni_3O_{10}$ crystals from (a). (c) a $La_4Ni_3O_{10}$ crystal ∼4.5 mm in length attached on Kapton tape and its diffraction patterns at various positions (d)–(n) ($\lambda = 0.117$ Å, 11-ID-C, APS; beam size $0.8 \times 0.8\,\mathrm{mm}^2$, scan step size 0.5 mm). Note that diffuse scattering is observed in the *hk*0 plane, reflecting some short-range deviation from the average structure. The vertical lines in (e)–(l) are artifacts caused by overexposure. The observation of multiple spots close together signifies twinning.

growth, consistent with reports of disordered intergrowths of different *n* members of Ruddlesden-Popper phases [18]. Traveling rates of 4–6 mm/h for the seed were found to be acceptable. The rotation speeds of feed and seed rods are related to the growth interface between solid and liquid, and a planar or slightly convex interface shape with respect to the growth crystal is reported to be desirable [55]. As demonstrated in Ref. [56] for floating zone growth of $Y_2Ti_2O_7$, the shape of the growth interface changes from convex to less convex, and finally to concave with the speed of rotation of the crystals decreasing from 30 to 7 rpm. In our crystal growth, we applied rotation speeds of 27 and 20 rpm for feed rod and seed, respectively, to achieve a stable melt zone and a convex growth front. Postgrowth cooling rate is an important parameter in obtaining the thermodynamically stable phase and/or trapping metastable phases if a material undergoes structural phase transition(s) on cooling. As reported by Nagell *et al.* [36], $La_4Ni_3O_{10}$ undergoes a series of phase transitions on cooling, from tetragonal to orthorhombic to monoclinic. We utilized two cooling rates after crystal growth: (i) keep traveling with fixed power, i.e., slow cooling, or (ii) power off immediately after separating feeding and seeding parts, i.e., rapid cooling. Method (i) was used to obtain the thermodynamically stable phase, and (ii) was used to trap a metastable phase.

A typical boule of $La_4Ni_3O_{10}$ is shown in Fig. 2(a). The growth direction is parallel to the *ab* plane. Crystals with shiny facets were cleaved from the as-grown boule, as shown in Fig. 2(b). Figure 2(c) shows a cleaved $La_4Ni_3O_{10}$ crystal, ∼4.5 mm in length. Diffraction patterns at various positions along the length of this crystal measured in transmission using synchrotron x rays ($\lambda = 0.1173$ Å) at beamline 11-ID-

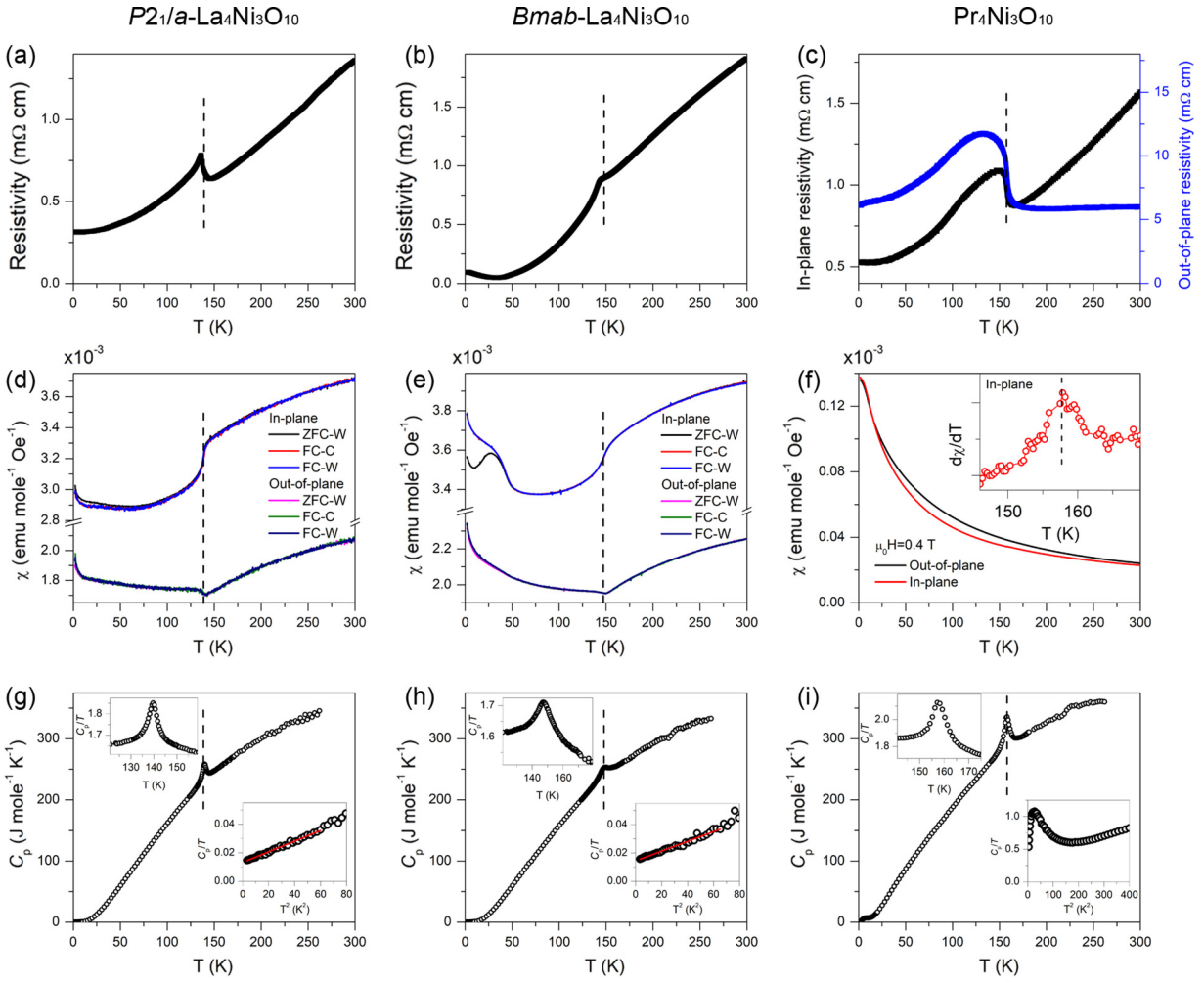

FIG. 3. Physical properties of $P2_1/a$, *Bmab* $La_4Ni_3O_{10}$, and $Pr_4Ni_3O_{10}$. (a), (d), (g) Resistivity, magnetic susceptibility, and heat capacity of $P2_1/a$ $La_4Ni_3O_{10}$. (b), (e), (h) Resistivity, magnetic susceptibility, and heat capacity of *Bmab* $La_4Ni_3O_{10}$. (c), (f), (i) Resistivity, magnetic susceptibility, and heat capacity of $Pr_4Ni_3O_{10}$.

C, Advanced Photon Source, are shown in Figs. 2(d)–2(n). The observation of the same diffraction pattern from position *d* to *l* indicates a large single crystal (i.e., coherent growth) with good crystallinity. The oxygen content of specimens randomly extracted from as-grown $La_4Ni_3O_{10}$ and $Pr_4Ni_3O_{10}$ boules was measured to be 9.98(1) and 10.05(1), respectively (see Fig. S2 of the Supplemental Material [39]). With deviation of $\leqslant$5 parts per 1000, both as-grown $La_4Ni_3O_{10}$ and $Pr_4Ni_3O_{10}$ are nominally stoichiometric.

B. Physical properties

Resistivity, magnetic susceptibility, and heat capacity were measured on as-grown $R_4Ni_3O_{10}$ (R = La, Pr) crystals. $La_4Ni_3O_{10}$ was found to exhibit two different phase transition temperatures depending on the postgrowth cooling: (i) T_{MMT} = 138.6 K using slow cooling rate after growth, and (ii) T_{MMT} = 147.5 K by rapid cooling the boule after growth. We will show below that the 138.6 K transition comes from a monoclinic ($P2_1/a$) phase and the 147.5 K transition from an orthorhombic (*Bmab*) phase (see Crystal Structure Determination). In contrast, $Pr_4Ni_3O_{10}$ shows a single T_{MMT} at 157.6 K, which is in the $P2_1/a$ phase. We will refer to these phases by their space group symmetry throughout this discussion of their physical properties.

Figures 3(a)–3(c) show the resistivity of $R_4Ni_3O_{10}$ as a function of temperature on warming. The in-plane resistivity drops with decreasing temperature from 300 K, indicating a metallic behavior. An anomaly was observed at 138.6, 147.5, and 157.6 K for $P2_1/a$-, *Bmab*-$La_4Ni_3O_{10}$, and $Pr_4Ni_3O_{10}$, respectively. To evaluate the anisotropy, the resistivity of $Pr_4Ni_3O_{10}$ was measured using the six-terminal method [48,49]. Its in-plane and out-of-plane resistivity at 300 K were measured to be 1.55 and 5.96 mΩ cm, respectively. The anisotropy at 300 K is 3.8, increasing to 11.7 at 2 K. Such an anisotropy is relatively small compared with other layered oxides such as manganites [48] and cuprates [57]. The temperature-dependent behavior of $R_4Ni_3O_{10}$ around the MMT resembles that of CDW materials such as chromium [58], purple bronzes [59], and rare-earth tritellurides [60].

The in-plane and out-of-plane magnetic properties of $R_4Ni_3O_{10}$ (R = La, Pr) were measured on single crystals under a magnetic field of 0.4 T [see Figs. 3(d)–3(f)] on warming and cooling. Because lanthanum is diamagnetic, we first look

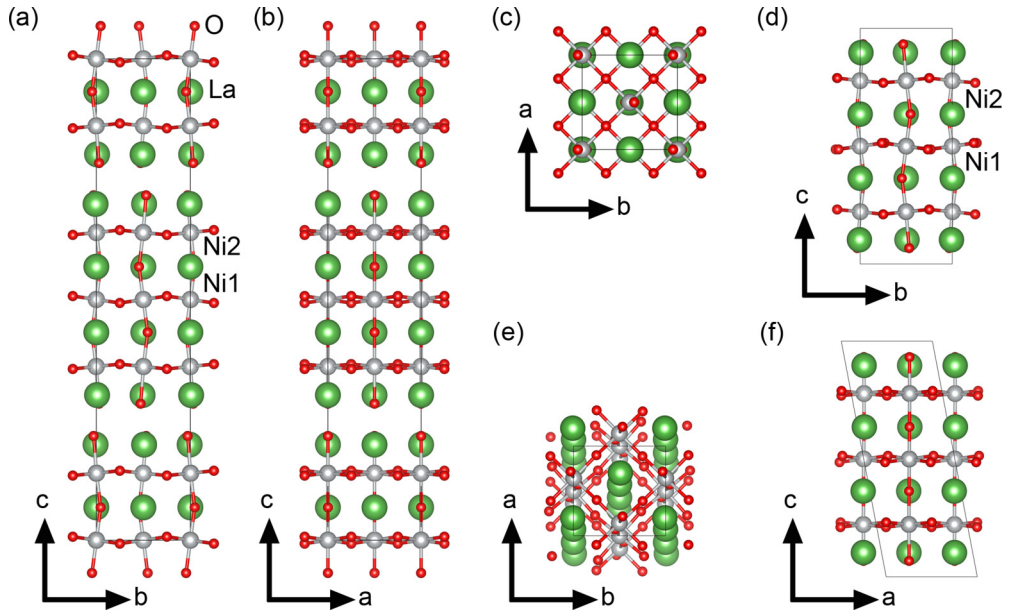

FIG. 4. Crystal structures and coordination environments of Ni atoms in $R_4Ni_3O_{10}$ (R = La, Pr) from single-crystal diffraction. (a)–(c) *Bmab* $La_4Ni_3O_{10}$; (d)–(f) $P2_1/a$ $La_4Ni_3O_{10}$.

at the case of $P2_1/a$ and *Bmab* $La_4Ni_3O_{10}$. Both the in-plane and out-of-plane magnetic susceptibility decrease on cooling above the MMT. Around the MMT, the *ab*-plane susceptibility sharply decreases with a decreasing temperature while the out-of-plane susceptibility reaches a minimum (at ∼141 K for $P2_1/a$ and at ∼149 K for *Bmab*), and then increases upon further cooling. Such behavior is neither Curie-Weiss nor Pauli [34], the latter expected of a metal. The lack of hysteresis between the warming and cooling processes indicates either a weakly first-order or a second-order transition. The magnetic susceptibility of $La_4Ni_3O_{10}$ is quite similar to CDW materials such as $K_{0.3}MoO_3$ [59], or spin density wave materials including $BaFe_2As_2$ [61]. We notice that *Bmab* $La_4Ni_3O_{10}$ shows an irreversibility below 50 K that can be connected to a weak ferromagnetic component, corroborated by isothermal $M(H)$ data (see Fig. S4 of the Supplemental Material [39]). Such a ferromagnetic behavior has been reported previously in oxidized $La_4Ni_3O_{10}$ [20]. The magnetic susceptibility of $Pr_4Ni_3O_{10}$ is Curie-Weiss-like due to the large contribution of the local paramagnetic moment from Pr^{3+}, which masks the underlying behavior of Ni moments. However, an anomaly is clearly seen in $d\chi/dT$ at 157.6 K, which is consistent with the anomaly seen in resistivity and

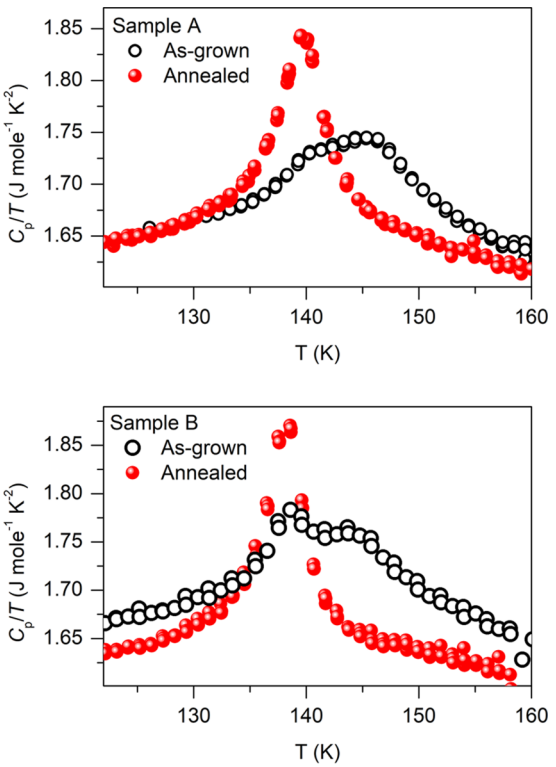

FIG. 5. Heat capacity of two specimens of as-grown biphasic $La_4Ni_3O_{10}$ before and after annealing. See text for details.

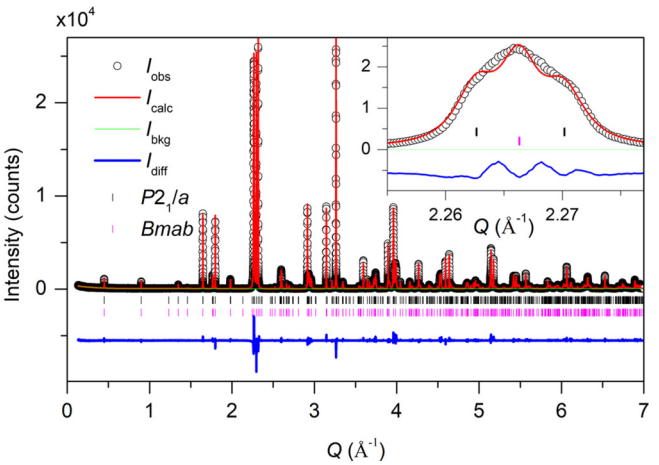

FIG. 6. High-resolution synchrotron x-ray powder diffraction pattern and Rietveld refinement of biphasic $La_4Ni_3O_{10}$. Insets show the quality of fit in the Q range 2.255–2.277 Å^{-1}.

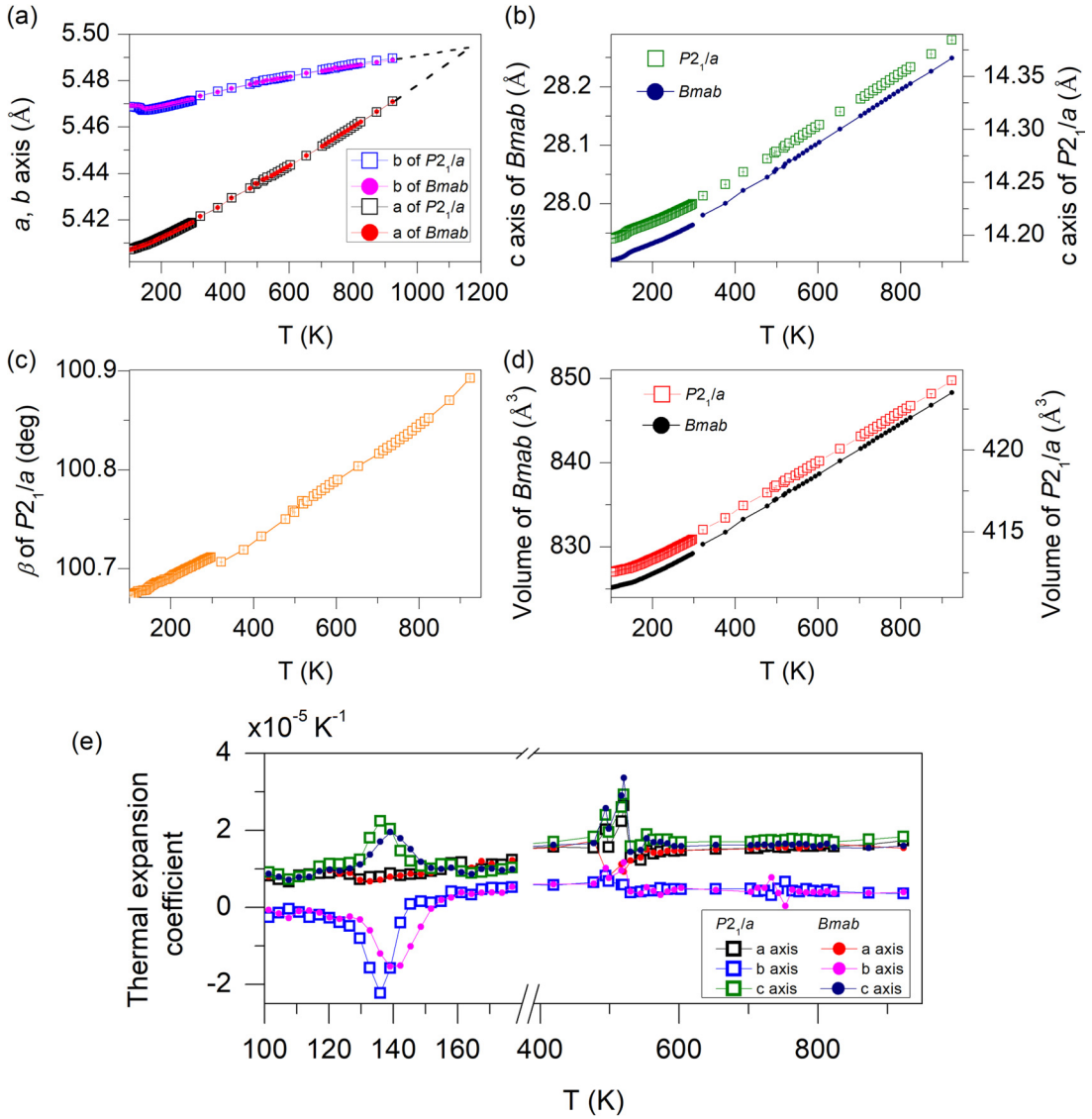

FIG. 7. Temperature dependence of lattice parameters of $La_4Ni_3O_{10}$ from 100 to 923 K obtained from Rietveld refinement of high-resolution synchrotron powder x-ray diffraction patterns. (a) a and b axes of $P2_1/a$ and $Bmab$ $La_4Ni_3O_{10}$. (b) c axis. (c) β of $P2_1/a$. (d) Volume. (e) Thermal expansion coefficients obtained from refined lattice parameters. Note the lattice parameters were obtained from two samples, one measured from 100 to 300 K, and the other measured from 321 to 923 K.

heat capacity. Huangfu *et al.* fitted χ to Curie-Weiss law below and above the transition, and reported a steplike feature in the magnetic susceptibility [23]. We performed high-resolution powder neutron diffraction on $R_4Ni_3O_{10}$ (R = La, Pr) to investigate whether the ground state is antiferromagnetic; however, no superlattice peaks were observed (see Fig. S5 of the Supplemental Material [39]). Later, our single-crystal neutron diffraction measurements unambiguously revealed weak magnetic superlattice reflections in addition to the main Bragg peaks, signaling a spin density wave below MMT [31].

The heat capacity of $P2_1/a$, $Bmab$ $La_4Ni_3O_{10}$, and $P2_1/a$ $Pr_4Ni_3O_{10}$ is shown in Figs. 3(g)–3(i). The phase transitions are clearly indicated by a prominent anomaly on each curve. To estimate the change of entropy across MMT, we have phenomenologically fit the behavior above and below with a polynomial and subtracted this background. The difference between C_p/T and the fit background is shown in Fig. S6 of the Supplemental Material [39]. Integrating the area under the resultant peak yields $\Delta S \sim 2.0\,\mathrm{J\,mole^{-1}\,K^{-1}}$ for $P2_1/a$ $La_4Ni_3O_{10}$, $\Delta S \sim 2.1\,\mathrm{J\,mole^{-1}\,K^{-1}}$ for $Bmab$ $La_4Ni_3O_{10}$, and $\Delta S \sim 2.7\,\mathrm{J\,mole^{-1}\,K^{-1}}$ for $Pr_4Ni_3O_{10}$ (see Fig. S6 of the Supplemental Material [39]). The entropy change is reported to be $1.5\mathrm{J\,mole^{-1}\,K^{-1}}$ for $P2_1/a$ $La_4Ni_3O_{10}$ by Kumar *et al.* [35], and $2.0\,\mathrm{J\,mole^{-1}\,K^{-1}}$ for $Pr_4Ni_3O_{10}$ by Huangfu *et al.* [23]. The insets of Figs. 3(g) and 3(h) show the C_p/T as a function of T^2 in the low-temperature region. The heat capacity at low temperature is fit to the standard model of the specific heat in a nonmagnetic solid, $C_p/T = \gamma + \beta T^2$, where γ is the electronic contribution and the T^2 term is from the lattice. The fit leads to $\gamma = 13.3\,\mathrm{mJ\,mole^{-1}\,K^{-2}}$ and $\beta = 3.7 \times 10^{-4}\,\mathrm{J\,mole^{-1}\,K^{-4}}$ for $P2_1/a$ $La_4Ni_3O_{10}$ [31] and $\gamma = 14.5\,\mathrm{mJ\,mole^{-1}\,K^{-2}}$ and $\beta = 3.4 \times 10^{-4}\,\mathrm{J\,mole^{-1}\,K^{-4}}$

for *Bmab* $La_4Ni_3O_{10}$. The extracted β values correspond to Debye temperatures of 450 [31] and 460 K, respectively. The obtained γ values are in good agreement with the previous report by Kumar *et al.* [35] and Wu *et al.* [62]. For $Pr_4Ni_3O_{10}$, a Schottky anomaly is observed at low temperature, indicating a manifold of relatively low-lying excited states probably due to crystal field splitting [63].

C. Crystal structure determination

As discussed in the Introduction, there is considerable debate about the ground-state crystal structure of $R_4Ni_3O_{10}$ materials. To address this lack of consensus, we turned to single-crystal x-ray diffraction on our specimens. We were able to isolate from the as-grown boule three different kinds of $La_4Ni_3O_{10}$ crystals: single-phase *Bmab*, single-phase $P2_1/a$, and mixed-phase $Bmab + P2_1/a$. For $Pr_4Ni_3O_{10}$, only $P2_1/a$ crystals were found. Using these crystals, we were able to establish that for both $R =$ La and Pr the room-temperature structure of $R_4Ni_3O_{10}$ is the monoclinic $P2_1/a$ structure with $Z = 2$ reported by Huangfu *et al.* [23]. Comprehensive details of the models tested and justification for selecting this monoclinic structure are provided (see Synchrotron x-ray single-crystal diffraction and Table S1 of the Supplemental Material [39]). Here we summarize the results.

Figure 4 shows the structures of *Bmab* and $P2_1/a$ $La_4Ni_3O_{10}$ in the *ab*, *bc*, and *ac* planes. Although the atomic arrangement in both the orthorhombic and monoclinic structures is the same—trilayer perovskitelike blocks separated by a rocksalt layer—the unit cell of *Bmab* consists of two such trilayers, while the $P2_1/a$ cell contains only one. For both *Bmab* and $P2_1/a$ $La_4Ni_3O_{10}$, La atoms are in 9 and 12 coordination with oxygen atoms, and Ni atoms are surrounded by 6 oxygen atoms, although the bond lengths are different (see Table II). It is worth noting that the outer Ni of the trilayer has a larger distortion of its oxygen octahedron than the inner Ni. This is not unusual for multilayer Ruddlesden-Popper phases, for instance, the bilayer manganite $La_{1.2}Sr_{1.8}MnO_7$ [64]. Bond valence sum calculations [65] were performed to evaluate the valence states of Ni. The obtained values of inner and outer Ni differ (3.0 vs 2.7; see Table II), reflecting charge differentiation between them. Such an observation has been discussed in $Pr_4Ni_3O_{10}$ [23] and $Nd_4Ni_3O_{10}$ [24].

Figure 5 shows the heat capacity of biphasic, as-grown samples of $La_4Ni_3O_{10}$, characterized by two anomalies that correspond to transitions in the $P2_1/a$ and *Bmab* phases. Figure 6 shows the high-resolution synchrotron x-ray powder diffraction pattern and Rietveld refinement of biphasic $La_4Ni_3O_{10}$ at room temperature. The refinement converged to $R_{wp} = 12.1\%$ and GOF (goodness of fit) $= 1.7$ with a mass fraction of 42.0 wt % for *Bmab* and 58.0 wt % for $P2_1/a$. The obtained lattice parameters are $a = 5.4193$ Å, $b = 5.4722$ Å, $c = 27.9656$ Å for *Bmab*, and $a = 5.4193$ Å, $b = 5.4717$ Å, $c = 14.2306$ Å, and $\beta = 100.712^\circ$ for $P2_1/a$. The inset of Fig. 6 shows the pattern and fit in the Q range 2.255–2.277 $Å^{-1}$, where three peaks are clearly seen, two outer peaks from $P2_1/a$ and an inner peak attributed to *Bmab*. Notably, the difference between $P2_1/a$ and *Bmab* is so subtle that lab x-ray diffraction cannot resolve it (see Fig. S3 of the Supplemental Material [39]).

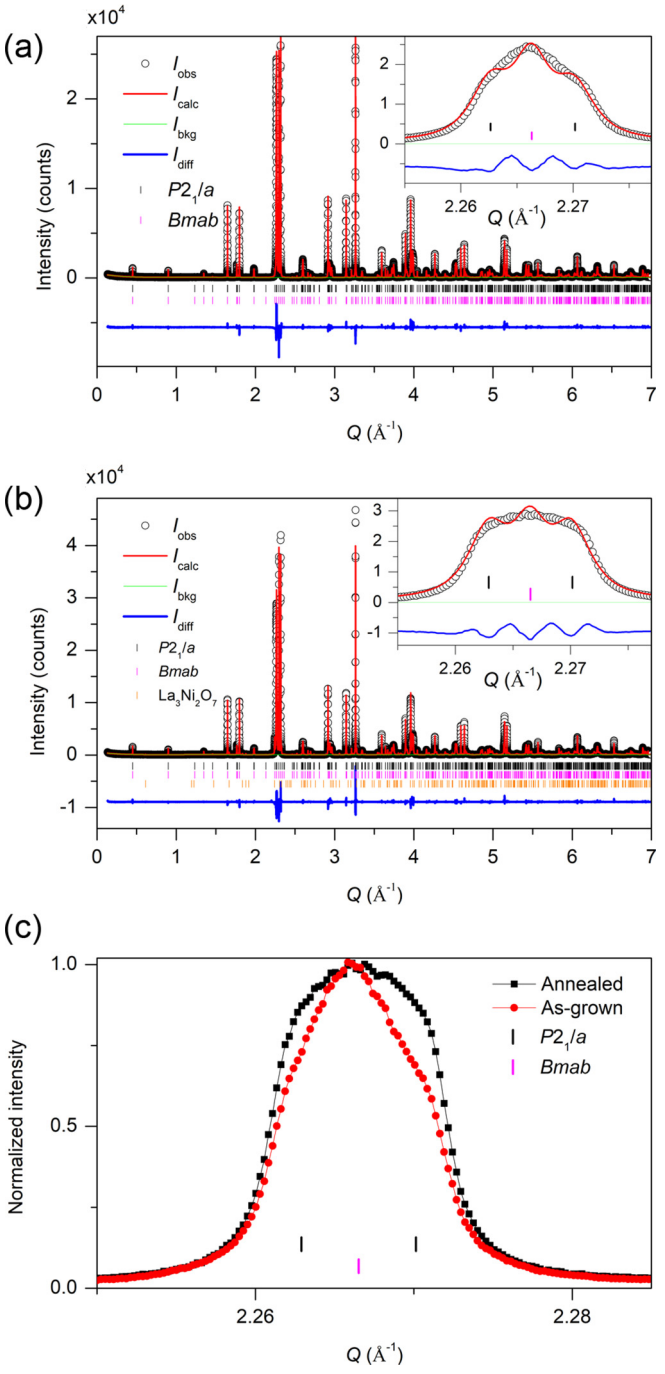

FIG. 8. Annealing effect on biphasic $La_4Ni_3O_{10}$. (a) High-resolution synchrotron x-ray powder diffraction pattern of as-grown $La_4Ni_3O_{10}$. (b) Annealed $La_4Ni_3O_{10}$ at 1 bar O_2. Insets show the quality of fit in Q range 2.255–2.277 $Å^{-1}$. (c) Comparison of the peaks before and after annealing in the range of $2.25 \leqslant Q \leqslant 2.285$ $Å^{-1}$ by normalizing their heights.

To link the crystal structures to their physical properties, we measured *in situ* high-resolution synchrotron x-ray powder diffraction on pulverized biphasic crystals of $La_4Ni_3O_{10}$ on cooling from 300 to 100 K. The evolution of the (200), (020), and (002) peaks as a function of temperature is shown in Fig. S7 of the Supplemental Material [39]. The shift of the peaks

TABLE III. Rietveld refinement result for as-grown and annealed bi-phasic $La_4Ni_3O_{10}$. Error bars represent the estimated standard deviations from the refinement.

	As-grown bi-phasic sample	After annealing
	$R_{wp} = 11.0\%$ and GOF = 2.0	$R_{wp} = 10.6\%$ and GOF = 2.3
$P2_1/a$ $La_4Ni_3O_{10}$	59.1% Mass fraction	68.6% Mass fraction
	$a = 5.4192(1)$ Å	$a = 5.4186(1)$ Å
	$b = 5.4716(1)$ Å	$b = 5.4711(1)$ Å
	$c = 14.2301(3)$ Å	$c = 14.2306(3)$ Å
	$\beta = 100.71(1)^\circ$	$\beta = 100.72(1)^\circ$
Bmab $La_4Ni_3O_{10}$	40.9% Mass fraction	28.0% Mass fraction
	$a = 5.4192(1)$ Å	$a = 5.4185(1)$ Å
	$b = 5.4721(1)$ Å	$b = 5.4712(1)$ Å
	$c = 27.9653(1)$ Å	$c = 27.9646(1)$ Å
$La_3Ni_2O_7$	0	3.4% Mass fraction
		$a = 5.3934(1)$ Å
		$b = 5.4497(1)$ Å
		$c = 20.5317(3)$ Å

towards higher 2θ on cooling indicates contraction of the unit cell above the MMT. No peak splitting or extra peaks were observed in the powder data below the MMT. Figure 7 presents the temperature dependence of the unit cell parameters a, b, c, β, and V extracted from Rietveld refinements, as well as the calculated linear thermal expansion coefficients. Anomalies are seen in the lattice parameters and linear thermal expansion coefficients at 138.6 and 147.5 K, corresponding to the monoclinic and orthorhombic phases, and reflecting lattice involvement in the MMTs. This response is particularly evident in the b axis. For $Pr_4Ni_3O_{10}$, an anomaly at 157.6 K is observed (see Figs. S8 and S9 of the Supplemental Material [39]). It is understandable how such a subtle lattice response, ≈0.03%, was missed previously [17,21].

We performed *in situ* high-resolution synchrotron x-ray powder diffraction on a mixed-phase sample on warming from 321 to 923 K in air to explore for a thermally driven transition in $La_4Ni_3O_{10}$ from $P2_1/a$ to *Bmab*. A monoclinic to orthorhombic transition was not observed. Indeed, over this temperature interval, the monoclinic β angle increases [Fig. 7(c)], showing no tendency toward higher symmetry. However, the Rietveld refinements show that the a and b axes of the orthorhombic phase are converging with warming and upon extrapolation would become metrically equivalent at ∼1160 K. Such an observation suggests the possibility of a transition to tetragonal phase, albeit at a significantly higher temperature than that reported by Nagell *et al.* (973 K) [36] and Amow *et al.* (758 K) [66]. If this is the case, it may indicate some difference in stoichiometry (presumably O content) between our sample and that of Nagell *et al.* [36] and Amow *et al.* [66]. The thermal expansion is anisotropic with smallest coefficient along the b axis. Anomalies at ∼550 and ∼750 K are observed, the former of which is consistent with the electronic transition seen in resistivity, magnetic susceptibility, and differential thermal analysis reported by Kobayashi *et al.* [19], and the latter of which is in agreement with the transition reported by Amow *et al.* [66] but with a different and as-yet unknown origin.

D. Thermodynamically stable phase of $R_4Ni_3O_{10}$

An open question is whether the true thermodynamic phase of $R_4Ni_3O_{10}$ at room temperature is *Bmab* or $P2_1/a$. Our biphasic crystals allow us to answer this question definitively. We annealed biphasic single crystals of $La_4Ni_3O_{10}$ under flowing oxygen at 1000 °C [67]. The heat capacity of the same specimen before and after annealing is presented in Fig. 5. The peak centered at 147.5 K (associated with the *Bmab* phase) becomes weaker after annealing, while the peak at 138.6 K (associated with the $P2_1/a$ phase) becomes more pronounced, reflecting a phase conversion from *Bmab* to $P2_1/a$. Such an observation has been reproduced in multiple samples. Figures 8(a) and 8(b) show the diffraction patterns of as-grown biphasic $La_4Ni_3O_{10}$ and the same sample after annealing. Figure 8(c) presents the region around $Q \sim 2.265$ Å^{-1} before and after annealing in flowing oxygen with peaks normalized. The increase of the intensity attributable to the $P2_1/a$ phase after annealing demonstrates a thermally driven conversion from *Bmab* to $P2_1/a$ and confirms that the latter is the thermodynamic stable state. This is shown quantitatively in Table III: The mass fraction of $P2_1/a$ increases while that of *Bmab* decreases, reflecting a conversion from *Bmab* to $P2_1/a$. That *Bmab* $Pr_4Ni_3O_{10}$ could be obtained by rapid cooling corroborates the metastability of the orthorhombic structure at room temperature (see Fig. S10 of the Supplemental Material [39]). We note that we cannot unequivocally rule out the possibility of a compositional change (e.g., O stoichiometry) during the annealing process. However, as shown in Table III, the lattice parameters are essentially unchanged (<1 part in 5000) compared to those before annealing, arguing that any such compositional change is most probably negligible.

IV. CONCLUSION

In summary, we successfully obtained single crystals of $La_4Ni_3O_{10}$ with two crystal structures (*Bmab* and $P2_1/a$) and $Pr_4Ni_3O_{10}$ ($P2_1/a$) using a high-pressure floating zone

furnace. Crystal structures of $R_4Ni_3O_{10}$ (R = La, Pr) have been determined by combining synchrotron and lab x-ray single-crystal diffraction, high-resolution synchrotron x-ray diffraction, and physical properties including resistivity, magnetic susceptibility, and heat capacity. Key outcomes of this work are (1) The monoclinic $P2_1/a$ ($Z = 2$) structure is established as the room-temperature thermodynamic state of both La- and $Pr_4Ni_3O_{10}$. For $La_4Ni_3O_{10}$, the $P2_1/a$ structure and a competing orthorhombic *Bmab* phase are apparently nearly degenerate, shedding light on past controversies over the crystallography of this material. (2) A weak, anisotropic lattice response was observed at the MMT, substantiating a lattice coupling to the electronic degrees of freedom. (3) Despite the weak lattice response at the MMT itself, the link between lattice and the electronic band structure is not insubstantial, with the MMT differing in $La_4Ni_3O_{10}$ by ≈ 10 K (7%) between the $P2_1/a$ and *Bmab* phases. Beyond this study, the availability of these $R_4Ni_3O_{10}$ (R = La, Pr) single crystals provides means to definitively test the CDW theory of the MMT [31], to test the theoretical prediction of $P2_1/a$ as the structure of its ground state [68], and to explore any putative analog between overdoped cuprates and nickelates in the framework of collective behavior exemplified by charge order.

ACKNOWLEDGMENTS

This work was supported by the U.S. Department of Energy, Office of Science, Basic Energy Sciences, Materials Science and Engineering Division. This research has been supported in part by ORNL Postdoctoral Development Fund by UT-Battelle, LLC under Contract No. DE-AC05-00OR22725 with the U.S. Department of Energy. The work at Shandong University was supported by the Qilu Young Scholars Program of Shandong University, and the Taishan Scholars Program of Shandong Province. NSF's ChemMatCARS Sector 15 is supported by the Divisions of Chemistry (CHE) and Materials Research (DMR), National Science Foundation, under Grant No. NSF/CHE-1834750. Use of the Advanced Photon Source, an Office of Science User Facility operated for the U.S. Department of Energy (DOE) Office of Science by Argonne National Laboratory, was supported by the U.S. DOE under Contract No. DE-AC02-06CH11357. J.Z. thanks Dr. Saul H. Lapidus for his help with the high-resolution powder diffraction experiment at 11-BM, and Dr. Raphael P. Hermann, Dr. D. Phelan, Dr. A. S. Botana, Dr. M. R. Norman, Dr. J. W. Freeland, Dr. V. Pardo, Dr. W. E. Pickett, and Dr. S. Rosenkranz for fruitful discussions.

[1] M. R. Norman, Materials design for new superconductors, Rep. Prog. Phys. **79**, 074502 (2016).

[2] J. M. Tranquada, Exploring intertwined orders in cuprate superconductors, Phys. B (Amsterdam, Neth.) **460**, 136 (2015).

[3] A. A. Kordyuk, Pseudogap from ARPES experiment: Three gaps in cuprates and topological superconductivity (Review Article), Low Temp. Phys. **41**, 319 (2015).

[4] B. Keimer, S. A. Kivelson, M. R. Norman, S. Uchida, and J. Zaanen, From quantum matter to high-temperature superconductivity in copper oxides, Nature **518**, 179 (2015).

[5] E. Fradkin, S. A. Kivelson, and J. M. Tranquada, Colloquium: Theory of intertwined orders in high temperature superconductors, Rev. Mod. Phys. **87**, 457 (2015).

[6] M. B. Salamon and M. Jaime, The physics of manganites: Structure and transport, Rev. Mod. Phys. **73**, 583 (2001).

[7] J. M. Tranquada, Spins, stripes, and superconductivity in hole-doped cuprates, in *Lectures on the Physics of Strongly Correlated Systems XVII: Seventeenth Training Course in the Physics of Strongly Correlated Systems*, AIP Conf. Proc. No. 1550 (AIP, Melville, NY, 2013), p. 114.

[8] H. Ulbrich and M. Braden, Neutron scattering studies on stripe phases in non-cuprate materials, Phys. C (Amsterdam, Neth.) **481**, 31 (2012).

[9] H. Miao, J. Lorenzana, G. Seibold, Y. Y. Peng, A. Amorese, F. Yakhou-Harris, K. Kummer, N. B. Brookes, R. M. Konik, V. Thampy, G. D. Gu, G. Ghiringhelli, L. Braicovich, and M. P. M. Dean, High-temperature charge density wave correlations in $La_{1.875}Ba_{0.125}CuO_4$ without spin-charge locking, Proc. Natl. Acad. Sci. USA **114**, 12430 (2017).

[10] Z. Sun, Q. Wang, A. V. Fedorov, H. Zheng, J. F. Mitchell, and D. S. Dessau, Localization of electrons due to orbitally ordered bistripes in the bilayer manganite $La_{2-2x}Sr_{1+2x}Mn_2O_7$($x \sim 0.59$), Proc. Natl. Acad. Sci. USA **108**, 11799 (2011).

[11] S. Anissimova, D. Parshall, G. D. Gu, K. Marty, M. D. Lumsden, S. Chi, J. A. Fernandez-Baca, D. L. Abernathy, D. Lamago, J. M. Tranquada, and D. Reznik, Direct observation of dynamic charge stripes in $La_{2-x}Sr_xNiO_4$, Nat. Commun. **5**, 3467 (2014).

[12] J. Zhang, Y. S. Chen, D. Phelan, H. Zheng, M. R. Norman, and J. F. Mitchell, Stacked charge stripes in the quasi-2D trilayer nickelate $La_4Ni_3O_8$, Proc. Natl. Acad. Sci. USA **113**, 8945 (2016).

[13] M. S. Senn, J. P. Wright, and J. P. Attfield, Charge order and three-site distortions in the Verwey structure of magnetite, Nature **481**, 173 (2011).

[14] M. Cwik, M. Benomar, T. Finger, Y. Sidis, D. Senff, M. Reuther, T. Lorenz, and M. Braden, Magnetic Correlations in $La_{2-x}Sr_xCoO_4$ Studied by Neutron Scattering: Possible Evidence for Stripe Phases, Phys. Rev. Lett. **102**, 057201 (2009).

[15] Y. Y. Peng, R. Fumagalli, Y. Ding, M. Minola, S. Caprara, D. Betto, M. Bluschke, G. M. De Luca, K. Kummer, E. Lefrançois, M. Salluzzo, H. Suzuki, M. Le Tacon, X. J. Zhou, N. B. Brookes, B. Keimer, L. Braicovich, M. Grilli, and G. Ghiringhelli, Re-entrant charge order in overdoped $(Bi, Pb)_{2.12}Sr_{1.88}CuO_{6+\delta}$ outside the pseudogap regime, Nat. Mater. **17**, 697 (2018).

[16] D. Li, K. Lee, B. Y. Wang, M. Osada, S. Crossley, H. R. Lee, Y. Cui, Y. Hikita, and H. Y. Hwang, Superconductivity in an infinite-layer nickelate, Nature **572**, 624 (2019).

[17] A. K. Tkalich, V. P. Glazkov, V. A. Somenkov, S. S. Shil'shtein, A. E. Kar'kim, and A. V. Mirmel'shtein, Synthesis, structure, and properties of nickelates $R_4Ni_3O_{10}$(R = Nd,Pr,La), Superconductivity **4**, 2280 (1991).

[18] Z. Zhang and M. Greenblatt, Synthesis, structure, and properties of $Ln_4Ni_3O_{10-\delta}$ (Ln = La, Pr, and Nd), J. Solid State Chem. **117**, 236 (1995).

[19] Y. Kobayashi, S. Taniguchi, M. Kasai, M. Sato, T. Nishioka, and M. Kontani, Transport and magnetic properties of $La_3Ni_2O_{7-\delta}$ and $La_4Ni_3O_{10-\delta}$, J. Phys. Soc. Jpn. **65**, 3978 (1996).

[20] M. D. Carvalho, M. M. Cruz, A. Wattiaux, J. M. Bassat, F. M. A. Costa, and M. Godinho, Influence of oxygen stoichiometry on the electronic properties of $La_4Ni_3O_{10\pm\delta}$, J. Appl. Phys. **88**, 544 (2000).

[21] C. D. Ling, D. N. Argyriou, G. Wu, and J. J. Neumeier, Neutron diffraction study of $La_3Ni_2O_7$: Structural relationships among $n = 1, 2$, and 3 phases $La_{n+1}Ni_nO_{3n+1}$, J. Solid State Chem. **152**, 517 (2000).

[22] M. Zinkevich, N. Solak, H. Nitsche, M. Ahrens, and F. Aldinger, Stability and thermodynamic functions of lanthanum nickelates, J. Alloys Compd. **438**, 92 (2007).

[23] S. Huangfu, G. D. Jakub, X. Zhang, O. Blacque, P. Puphal, E. Pomjakushina, F. O. von Rohr, and A. Schilling, Anisotropic character of the metal-to-metal transition in $Pr_4Ni_3O_{10}$, Phys. Rev. B **101**, 104104 (2020).

[24] B.-Z. Li, C. Wang, Y.-B. Liu, J. Wu, Z. Ren, G.-M. Zhang, and G.-H. Cao, Metal-to-metal transition and heavy-electron state in $Nd_4Ni_3O_{10-\delta}$, Phys. Rev. B **101**, 195142 (2020).

[25] D. K. Seo, W. Liang, M. H. Whangbo, Z. Zhang, and M. Greenblatt, Electronic band structure and madelung potential study of the nickelates La_2NiO_4, $La_3Ni_2O_7$, and $La_4Ni_3O_{10}$, Inorg. Chem. **35**, 6396 (1996).

[26] M. Greenblatt, Z. Zhang, and M. H. Whangbo, Electronic properties of $La_3Ni_2O_7$ and $Ln_4Ni_3O_{10}$, Ln = La, Pr and Nd, Synth. Met. **85**, 1451 (1997).

[27] M. D. Carvalho, F. M. A. Costa, I. D. S. Pereira, A. Wattiaux, J. M. Bassat, J. C. Grenier, and M. Pouchard, New preparation method of $La_{n+1}Ni_nO_{3n+1-\delta}$ ($n = 2, 3$), J. Mater. Chem. **7**, 2107 (1997).

[28] M. Zinkevich and F. Aldinger, Thermodynamic analysis of the ternary La-Ni-O system, J. Alloys Compd. **375**, 147 (2004).

[29] J. Zhang, A. S. Botana, J. W. Freeland, D. Phelan, H. Zheng, V. Pardo, M. R. Norman, and J. F. Mitchell, Large orbital polarization in a metallic square-planar nickelate, Nat. Phys. **13**, 864 (2017).

[30] J. Zhang, D. M. Pajerowski, A. S. Botana, H. Zheng, L. Harriger, J. Rodriguez-Rivera, J. P. C. Ruff, N. J. Schreiber, B. Wang, Y.-S. Chen, W. C. Chen, M. R. Norman, S. Rosenkranz, J. F. Mitchell, and D. Phelan, Spin Stripe Order in a Square Planar Trilayer Nickelate, Phys. Rev. Lett. **122**, 247201 (2019).

[31] J. Zhang, D. Phelan, A. S. Botana, Y.-S. Chen, H. Zheng, M. Krogstad, S. G. Wang, Y. Qiu, J. A. Rodriguez-Rivera, R. Osborn, S. Rosenkranz, M. R. Norman, and J. F. Mitchell, Intertwined density waves in a metallic nickelate, arXiv:2004.07897.

[32] V. I. Voronin, I. F. Berger, V. A. Cherepanov, L. Y. Gavrilova, A. N. Petrov, A. I. Ancharov, B. P. Tolochko, and S. G. Nikitenko, Neutron diffraction, synchrotron radiation and EXAFS spectroscopy study of crystal structure peculiarities of the lanthanum nickelates $La_{n+1}Ni_nO_y$ (n = 1,2,3), Nucl. Instrum. Methods Phys. Res., Sect. A. **470**, 202 (2001).

[33] A. Olafsen, H. Fjellvåg, and B. C. Hauback, Crystal structure and properties of $Nd_4Co_3O_{10+\delta}$ and $Nd_4Ni_3O_{10-\delta}$, J. Solid State Chem. **151**, 46 (2000).

[34] M. U. Nagell, S. Kumar, M. H. Sørby, H. Fjellvåg, and A. O. Sjåstad, Structural and magnetic aspects of $La_4(Co_{1-x}Ni_x)_3O_{10+\delta}$ ($0 \leqslant x \leqslant 1$), Phase Transitions **88**, 979 (2015).

[35] S. Kumar, Ø. Fjellvåg, A. O. Sjåstad, and H. Fjellvåg, Physical properties of Ruddlesden-Popper ($n = 3$) nickelate: $La_4Ni_3O_{10}$, J. Magn. Magn. Mater. **496**, 165915 (2020).

[36] M. U. Nagell, W. A. Sławiński, P. Vajeeston, H. Fjellvåg, and A. O. Sjåstad, Temperature induced transitions in $La_4(Co_{1-x}Ni_x)_3O_{10+\delta}$: Oxygen stoichiometry and mobility, Solid State Ionics **305**, 7 (2017).

[37] S. Huangfu, X. Zhang, and A. Schilling, Correlation between the tolerance factor and phase transition in $Ln_{4-x}Ln'_xNi_3O_{10}$ (Ln and $Ln' = La$, Pr and Nd; $x = 0$, 1, 2 and 3), arXiv:2003.08478.

[38] W. A. Phelan, J. Zahn, Z. Kennedy, and T. M. McQueen, Pushing boundaries: High pressure, supercritical optical floating zone materials discovery, J. Solid State Chem. **270**, 705 (2018).

[39] See Supplemental Material at http://link.aps.org/supplemental/10.1103/PhysRevMaterials.4.083402 for supplemental figures and tables.

[40] Bruker APEX2, (Bruker Analytical X-ray Instruments Inc., Madison, WI, 2014).

[41] G. M. Sheldrick, Computer code SHELXTL (Bruker Analytical X-ray Instruments Inc., Madison, WI, 2001).

[42] https://www.ccdc.cam.ac.uk/structures/.

[43] B. H. Toby and R. B. Von Dreele, GSAS-II: the genesis of a modern open-source all purpose crystallography software package, J. Appl. Crystallogr. **46**, 544 (2013).

[44] S. Torii, M. Yonemura, Y. Ishikawa, P. Miao, R. Tomiyasu, S. Satoh, Y. Noda, and T. Kamiyama, Improvement of instrument devices for super high resolution powder diffractometer at J-PARC, J. Phys.: Conf. Ser. **502**, 012052 (2014).

[45] S. Torii, M. Yonemura, T. Yulius Surya Panca Putra, J. Zhang, P. Miao, T. Muroya, R. Tomiyasu, T. Morishima, S. Sato, H. Sagehashi, Y. Noda, and T. Kamiyama, Super high resolution powder diffractometer at J-PARC, J. Phys. Soc. Jpn. **80**, SB020 (2011).

[46] R. Oishi, M. Yonemura, Y. Nishimaki, S. Torii, A. Hoshikawa, T. Ishigaki, T. Morishima, K. Mori, and T. Kamiyama, Rietveld analysis software for J-PARC, Nucl. Instrum. Methods Phys. Res., Sect. A **600**, 94 (2009).

[47] R. Oishi-Tomiyasu, M. Yonemura, T. Morishima, A. Hoshikawa, S. Torii, T. Ishigaki, and T. Kamiyama, Application of matrix decomposition algorithms for singular matrices to the Pawley method in Z-Rietveld, J. Appl. Crystallogr. **45**, 299 (2012).

[48] Q. A. Li, K. E. Gray, and J. F. Mitchell, Spin-independent and spin-dependent conductance anisotropy in layered colossal-magnetoresistive manganite single crystals, Phys. Rev. B **59**, 9357 (1999).

[49] G. A. Levin, On the theory of measurement of anisotropic electrical resistivity by flux transformer method, J. Appl. Phys. **81**, 714 (1997).

[50] J. Zhang, H. Zheng, Y.Ren, and J. F. Mitchell, High-pressure floating-zone growth of perovskite nickelate $LaNiO_3$ single crystals, Cryst. Growth Des. **17**, 2730 (2017).

[51] B.-X. Wang, S. Rosenkranz, X. Rui, J. Zhang, F. Ye, H. Zheng, R. F. Klie, J. F. Mitchell, and D. Phelan, Antiferromagnetic

defect structure in $LaNiO_{3-\delta}$ single crystals, Phys. Rev. Mater. **2**, 064404 (2018).

[52] H. Guo, Z. W. Li, L. Zhao, Z. Hu, C. F. Chang, C.-Y. Kuo, W. Schmidt, A. Piovano, T. W. Pi, O. Sobolev, D. I. Khomskii, L. H. Tjeng, and A. C. Komarek, Antiferromagnetic correlations in the metallic strongly correlated transition metal oxide $LaNiO_3$, Nat. Commun. **9**, 43 (2018).

[53] K. Dey, W. Hergett, P. Telang, M. M. Abdel-Hafiez, and R. Klingeler, Magnetic properties of high-pressure optical floating-zone grown $LaNiO_3$ single crystals, J. Cryst. Growth **524**, 125157 (2019).

[54] H. Zheng, J. Zhang, B. Wang, D. Phelan, M. J. Krogstad, Y. Ren, W. A. Phelan, O. Chmaissem, B. Poudel, and J. F. Mitchell, High pO_2 floating zone crystal growth of the perovskite nickelate $PrNiO_3$, Crystals **9**, 324 (2019).

[55] S. M. Koohpayeh, D. Fort, and J. S. Abell, The optical floating zone technique: A review of experimental procedures with special reference to oxides, Prog. Cryst. Growth Charact. Mater. **54**, 121 (2008).

[56] C. Liu, A. Dabkowski, W.-Q. Jie, B. D. Gaulin, and H. A. Dabkowska, Optical observation of striations in $Y_2Ti_2O_7$ single crystals, Crystals **9**, 233 (2019).

[57] V. Hardy, A. Maignan, C. Martin, F. Warmont, and J. Provost, Anisotropy of resistivity in Tl-based single crystals: Direct evidence for the influence of the blocking-layer thickness and correlation with superconducting properties, Phys. Rev. B **56**, 130 (1997).

[58] E. Fawcett, Spin-density-wave antiferromagnetism in chromium, Rev. Mod. Phys. **60**, 209 (1988).

[59] M. Greenblatt, Molybdenum oxide bronzes with quasi-low-dimensional properties, Chem. Rev. **88**, 31 (1988).

[60] D. A. Zocco, J. J. Hamlin, K. Grube, J. H. Chu, H. H. Kuo, I. R. Fisher, and M. B. Maple, Pressure dependence of the charge-density-wave and superconducting states in $GdTe_3$, $TbTe_3$, and $DyTe_3$, Phys. Rev. B **91**, 205114 (2015).

[61] P. C. Canfield and S. L. Bud'ko, FeAs-based superconductivity: A case study of the effects of transition metal doping on $BaFe_2As_2$, Annu. Rev. Condens. Matter Phys. **1**, 27 (2010).

[62] G. Q. Wu, J. J. Neumeier, and M. F. Hundley, Magnetic susceptibility, heat capacity, and pressure dependence of the electrical resistivity of $La_3Ni_2O_7$ and $La_4Ni_3O_{10}$, Phys. Rev. B **63**, 245120 (2001).

[63] E. McCalla, D. Phelan, M. J. Krogstad, B. Dabrowski, and C. Leighton, Electrical transport, magnetic, and thermodynamic properties of La-, Pr-, and Nd-doped $BaSnO_{3-\delta}$ single crystals, Phys. Rev. Mater. **2**, 084601 (2018).

[64] J. F. Mitchell, D. N. Argyriou, J. D. Jorgensen, D. G. Hinks, C. D. Potter, and S. D. Bader, Charge delocalization and structural response in layered $La_{1.2}Sr1_{.8}Mn_2O_7$: Enhanced distortion in the metallic regime, Phys. Rev. B **55**, 63 (1997).

[65] A. Altomare, C. Cuocci, C. Giacovazzo, A. Moliterni, R. Rizzi, N. Corriero, and A. Falcicchio, EXPO2013: A kit of tools for phasing crystal structures from powder data, J. Appl. Crystallogr. **46**, 1231 (2013).

[66] G. Amow, I. J. Davidson, and S. J. Skinner, A comparative study of the Ruddlesden-Popper series, $La_{n+1}Ni_nO_{3n+1}$ ($n = 1$, 2 and 3), for solid-oxide fuel-cell cathode applications, Solid State Ionics **177**, 1205 (2006).

[67] We performed additional annealing experiments in an attempt to isolate the high-temperature tetragonal phase of $La_4Ni_3O_{10}$; however, we did not find evidence for this tetragonal phase (see Fig. S11 of the Supplemental Material [39]).

[68] D. Puggioni and J. M. Rondinelli, Crystal structure stability and electronic properties of the layered nickelate $La_4Ni_3O_{10}$, Phys. Rev. B **97**, 115116 (2018).